Influence of a 'Step' on the liquid–liquid flow patterns and flow phenomena in a microfluidic Y-Y channel

Sudha, Anand; Santoso, Albert; Rohde, Martin

DOI
10.1016/j.cej.2025.161823

Publication date
2025

Document Version
Final published version

Published in
Chemical Engineering Journal

Chemical Engineering Journal 512 (2025) 161823

Contents lists available at ScienceDirect

Chemical Engineering Journal

journal homepage: www.elsevier.com/locate/cej

Influence of a 'Step' on the liquid–liquid flow patterns and flow phenomena in a microfluidic Y-Y channel

Anand Sudha [a],*, Albert Santoso [b], Martin Rohde [a]

[a] Department of Radiation Science and Technology, Technical University of Delft, Mekelweg 5 2628 CD Delft, The Netherlands
[b] Department of Chemical Engineering, Technical University of Delft, Van Der Maasweg 9, 2629 HZ Delft, The Netherlands

ARTICLE INFO

Keywords:
Microfluidics
Multiphase flow
Liquid-liquid extraction
Flow maps
Flow separation
Flow patterns

ABSTRACT

Microfluidic multiphase flows are being increasingly used in many mass transfer applications because of the numerous advantages of operating in the microscale such as greater flow stability and low cost. Among the various flow regimes, parallel flow in the microscale is considered to be advantageous for extraction applications, especially radioisotope transfer, because efficient transfer and purification are possible as long as the interface position remains stable throughout without leakage at the outlets. Therefore, some papers have worked with asymmetric microchannels with different depths for the two fluids in mass transfer applications. The flow phenomena in such channels, however, have not been studied in detail. This paper focuses on these asymmetric microchannels, which we have termed 'step' channels, and the influence such an asymmetry has on the flow phenomena. We perform experiments on this channel and compare the flow maps with experiments in a channel of uniform depth (standard channel). The step channel was found to favour parallel flow and interestingly, to produce stable parallel flow without leakage at low Capillary numbers. This is contrary to the results observed in a standard channel, where slug flow is observed. Volume-of-fluid simulations showed the role of interfacial tension in obtaining stable parallel flow in a step channel. Additionally, flow maps were also plotted for step channels of different widths and degrees of asymmetry, where it was found that smaller widths and higher degrees of asymmetry favour stable parallel flow.

1. Introduction

Liquid–Liquid two-phase flows are commonly used in many industrial applications such as oil and gas [1], medicine [2], metal extraction [3], chemistry [4] and handling of industrial effluents [5]. It is particularly important in both the transport and extraction of substances from one fluid and to another fluid. Working with such fluids in the macroscale brings its own challenges — difficult transport, lower surface–volume ratios and instabilities observed even for laminar flows. These limitations can be largely overcome by operating in the microscale as microfluidic flows are generally controllable, amenable to automation and cost-effective [6–8]. Two-phase flow patterns have been studied in microfluidic channels of various geometries - Y-Y [9,10], T-T [11], serpentine [12] and cross junction channels [13].

The flow patterns are governed by several factors such as the interfacial tension, fluid viscosities, wettabilities, flow velocities, and, channel dimensions and geometry [9]. While the overall flow patterns vary from case to case, they can commonly be described in terms of three regimes — slug flow, where one fluid is dispersed in the form of droplets or slug in another, parallel flow, where the fluids flow parallel to each other and a transitional regime (or regimes) which combines the characteristics of both these regimes [9,14,15]. These flow regimes are dependent on multiple forces, whose inter-relation can be described by three dimensionless numbers [16]:

$$\begin{aligned} \mathrm{Ca} &= \frac{u\mu}{\sigma} \\ \mathrm{We} &= \frac{\rho u^2 D}{\sigma} \\ \mathrm{Re} &= \frac{\rho u D}{\mu} \end{aligned} \tag{1}$$

where Ca, We and Re are the Capillary, Weber, and Reynolds numbers respectively, ρ is the fluid density, u is the fluid velocity, μ the fluid viscosity, D the characteristic length of the channel and σ is the interfacial tension coefficient. Generally, slug flow occurs when the interfacial forces are strong, i.e., when the Ca and We are low, and parallel flow occurs when the inertial forces are high or when Ca, We or Re are high [17].

One of the applications where microfluidic multiphase flow is very important is Liquid–Liquid Extraction (LLE) [18]. Here, a substance

* Corresponding author.
E-mail addresses: A.Sudha-1@tudelft.nl (A. Sudha), M.Rohde@tudelft.nl (M. Rohde).

https://doi.org/10.1016/j.cej.2025.161823
Received 4 November 2024; Received in revised form 21 February 2025; Accepted 19 March 2025
Available online 10 April 2025

is transferred from one fluid to another when these fluids interact with each other [3]. Both slug and parallel flow are used for this purpose, but in the case of radioisotopes and Continuous Flow Chemical Processing (CFCP), parallel flow is especially important [19]. This is because parallel flow with the interface located exactly at the centre of the channel eliminates the need to separate the fluids after the material transfer, and this is especially useful to save time and obtain high purity for radioisotopes with low half-lives [18]. Many papers have studied interface stability and the conditions necessary for stable parallel flow [20–22].

To ensure stable parallel flow with easy flow separation, some papers suggest adding phase guides to the channel to guide the fluid motion [23], some modify the outlet geometry [24] and others tend to coat the channel accordingly to modify the wettabilities [25]. All these methods have their drawbacks, with phase guides not providing stable parallel flow for long periods [26], the modified outlet leading to a loss of fluid [24] and the channel coatings being applicable only for a specific set of fluids and cannot be used for all cases. Coatings are especially a problem for studies involving radionuclides as many of them break down under radiation.

One suggestion is to modify the overall geometry of the channel, and a design that has been used in literature for LLE purposes involves using an asymmetric microchannel with different depths for the two fluids [19,27,28]. We call this design the 'step' design as the presence of a shallow and deep part resembles a step (Fig. 1(b)). This channel has been found to be particularly effective in obtaining stable, parallel flow [29].

Flow patterns have been extensively studied in microchannels of various geometries such as Y-shaped channel [10,11,30,31], T-shaped channel [10,11,32,33] and cross-junction channel [13,34,35]. Generally, these studies observed the effect of the dimensionless numbers mentioned in Eq. (1) on the flow regimes. Some papers, like those of Kashid et al. [11] and Asadi-Sanghandi et al. [12], tried developing generalized flow maps to describe flow regimes for all possible fluids and geometries.

However, all these studies have been conducted on channels of symmetric cross-section (standard design). Papers which have studied the influence of channel geometry have limited their research to channel dimensions and inlet geometry [10,11]. To the authors' knowledge, no studies have been conducted on the effect of the step on the flow patterns. Considering the utility of the step channel in multiple LLE applications, it is imperative to understand the effect such a modification might have on the flow phenomena. Studying the flow patterns for such a step channel and comparing it to a channel with a symmetric cross section will, thus, not only expand the application of such microfluidic channels in LLE, but also enhance our understanding of the influence of channel geometry on fluid flow. This is especially important when we consider the use of such channels in radioisotope extraction studies.

Therefore, this study focuses on understanding the nature of the flow phenomena in such a step design and, the influence of channel dimensions and geometry on two-phase flow. The flow patterns obtained from this design will be compared with the corresponding results obtained from the commonly used channel with a symmetric cross-section experimentally. Volume-of-fluid (VOF) simulations are used to understand the differences in flow regimes observed in the step and standard channels. Further, the effect of the channel dimensions and the extent of asymmetry on the flow phenomena in a Step channel will also be studied.

The paper is organized as follows. The experimental and simulation methodologies are described in Section 2, along with the fluid properties and flow initialization. Section 3 observes the different flow phenomena in a step and standard channel, which include the flow regimes, flow maps and VoF simulations. Flow phenomena are then studied in step channels of varying widths in Section 4 and generalized flow maps are proposed in Section 5. Finally, the paper is concluded in Section 6.

2. Methods and materials

2.1. PDMS microfluidic chip fabrication

Microfluidic chips could be fabricated using different materials. As it is important to modify the geometry of the chips, polydimethylsiloxane (PDMS) is used because the chips can be easily manufactured. PDMS is an organosilicon polymer that stays in liquid form upon mixing the elastomers with the curing agent. As a result, the mixture can be poured into a petri dish with a patterned mould master, where it takes the shape of the pattern printed on the mould master. The petri dish can be set in an oven to speed up the hardening process.

To fabricate the microfluidic chip, we first fabricated the mould master using the soft lithography technique. On top of a cleaned 4 inch silicon wafer, we spin-coated a negative photoresist (SU8-2050, micro resist technology GmbH) at 2000 rpm for 30 s to obtain a layer of 50 μm thickness. The wafer was then baked at 100 °C for 15 min and loaded onto LaserWriter (Heidelberg, 1 μm laser beam at 365 nm). In the LaserWriter, we converted a bottom pattern (Y-Y shape, width from 250–1000 μm, Fig. 1(a)), designed using Autocad 2019 (Autodesk). The pattern was then written on the wafer. Afterwards, the wafer was soft-baked at 100 °C for 5 min.

To deposit another layer, we spin-coated another negative photoresist. To obtain an additional 25 μm and 50 μm we used SU8-2025 and SU8-2050 accordingly, with similar spin-coating parameters. After the second spin-coating, the wafer was baked at 100 °C for 15 min and reloaded onto the LaserWriter where a top pattern (half-channel, refer to Fig. 1(b)) was converted, aligned, and written. The wafer was soft-baked again at 100 °C for 5 min. Thereafter, the wafer was developed using Propylene glycol methyl ether acetate (> 99.5%, Merck Sigma) for 10 min, and post-baked at 200 °C for 30 min.

The PDMS microfluidic chip was fabricated by mixing the elastomer (Sylgard 184 Elastomer Kit, Dow Corning Comp.) and the curing agent with a mass ratio of 10:1. The mixture was then degassed, poured over the patterned master mould on a petri dish, and cured at 70 °C for 10 h. The hardened PDMS chips were gently removed from the mould master and cut to size. The inlets and outlets were punched using a 1.5 mm biopsy puncher, before being cleaned using ethanol. On the other hand, a glass slide was spin-coated with 20 μm PDMS (2000 rpm for 2 min, Laurell WS-650-23B). Both the chips and the coated glass slides were bonded together using oxygen plasma treatment (Harrick PDC-002) at 0.2–0.4 mbar for 140 s.

2.2. Fluid properties and flow setup

To conduct the flow experiments, we used two syringe pumps (Pump 11 Pico Plus Elite). On each of the syringe pumps, a 10 mL syringe (Beckton-Dickinson, Discardit II) was mounted. One of the syringes contained demineralized water with 10 mg/L brilliant blue dye while the other syringe contained an immiscible fluorinated oil (HydroFluoroEther, HFE, 3M™ Novec™ 7500 Engineered Fluid). The syringes were connected with PEEK tubes (0.5 mm ID, 1.59 mm OD, 300 mm in length) to the inlets of the microfluidic chips. The outlets were connected to other PEEK tubes, leading to a disposal container.

The fluid properties are given in Table 1. The contact angle corresponds to the angle made by the Novec–Water interface on the PDMS chip, and in our case, PDMS was observed to be hydrophobic.

2.3. Channel geometry and dimensions

Each of the channels in the experiments has a Y-Y geometry as shown in Fig. 1(a). In the case of the standard design, the depth remains uniform throughout, whereas, in the step design, half of the channel has one depth and the other half has another depth as shown in Fig. 1(b).

Five different channels are used here — one standard and four step channels. Two geometrical dimensions are varied in the case of the step channel — the width (W) and the step ratio $\lambda = \frac{H_1}{H_2}$. The dimensions of the channels are described in Table 2.

Table 1
Fluid properties.

Fluid	Density (kg/m^3)	Viscosity (mPas)	Surface tension (mN/m)	Contact angle (°)
Water	997	1.01	43.8	–
HFE/Novec™ 7500	1614	1.24	–	39.7

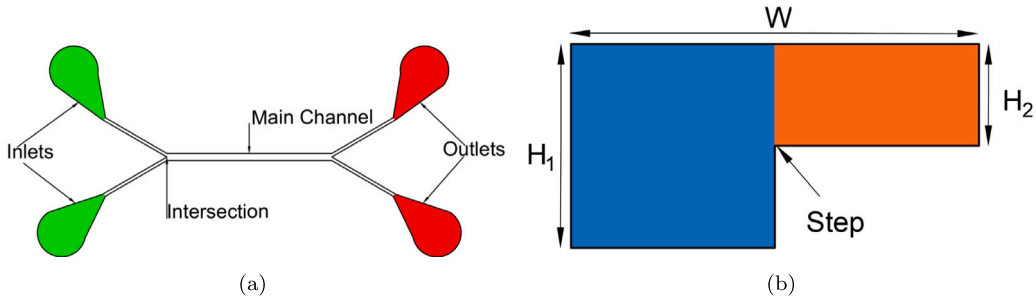

Fig. 1. Channel geometry. (a) Y-Y, with two inlets and outlets (b) Step design with two depths for each half of the channel.

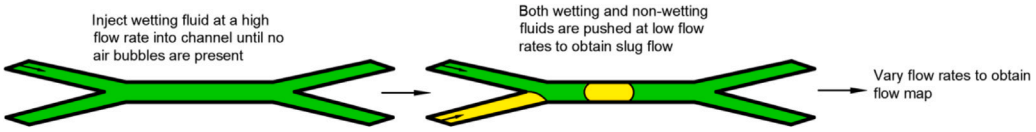

Fig. 2. Initialization Procedure in the Standard Channel. The green fluid is the wetting fluid and the yellow fluid is the non-wetting fluid.

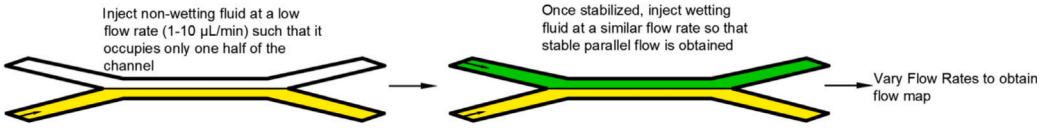

Fig. 3. Initialization Procedure in the Step Channel. The green fluid is the wetting fluid and the yellow fluid is the non-wetting fluid.

Table 2
Channel dimensions used throughout this work. The height of the shallower section is fixed at 50 μm as the height of the deeper section is varied.

Number	Length (cm)	W (μm)	H_1 (μm)	λ
1 (Standard)	1.2	500	50	1
2	1.2	500	100	2
3	1.2	250	100	2
4	1.2	1000	100	2
5	1.2	500	75	1.5

2.4. Flow initialization

Since the flow phenomena in the microscale are very sensitive to air bubbles, care must be taken to ensure proper initialization [36]. In the case of the standard channel, initializing with parallel flow will make it harder to achieve slug flow at lower flow rates (Fig. 2). To ensure repeatable results for all the flow regimes and to prevent air bubbles from entering, we initialize the experiments by filling the channel with the more wettable fluid, in this case, Novec, at a high flow rate of 100–150 μL/min. In case any air bubbles enter, they are flushed out first before allowing water to enter. Then, the flow rates of Novec and water are adjusted to the desired Capillary number and then the experiments are performed.

For the step channel, the initialization procedure is different. Here, the fluid with lower viscosity has to occupy the shallower channel, otherwise, viscous instabilities occur which make it difficult to obtain reproducible flow maps. Large flow rate ratios are then necessary to obtain stable parallel flow [28]. As the channel has an asymmetric cross-section, any air bubbles or liquid droplets can hinder the flow and cause some instabilities, making it difficult to obtain stable parallel flow.

Therefore, we initialize in such a way that water occupies the shallow section and Novec the deep section, and then vary the flow rates to create a flow map as shown in Fig. 3. Initializing at a high flow rate will lead to water wetting the entire channel, both the shallow and deep parts. Repeatable and reproducible results cannot be obtained once this happens. The problems associated with high flow rate initialization can be seen in Fig. 4. Water occupies the entire channel at first, but because it is the non-wetting fluid, Novec occupies the regions near the channel walls. This leads to a mixed regime where both fluids occupy both sections regardless of the flow rate. Thus, no repeatable flow map can be obtained.

To ensure repeatable results, we first introduce water into the shallow section at a low flow rate (1–10 μL/min) and then introduce Novec into the deeper section at a similar flow rate. Once we observe stable parallel flow, we then proceed to vary the flow rates according to the desired regimes.

2.5. VOF simulations

Fluid flow is simulated using Ansys Fluent 2022 R2. The individual fluid flow is simulated using the Navier–Stokes equation [37]. A volume fraction is defined and a volume fraction continuity equation is solved to track the position of the interface. The density and viscosity of the two-phase mixture are described by:

$$\rho = \alpha\rho_1 + (1-\alpha)\rho_2$$
$$\mu = \alpha\mu_1 + (1-\alpha)\mu_2 \quad (2)$$

where ρ and μ are the density and viscosity of the mixture respectively, α is the volume fraction of liquid 1. The surface tension is included

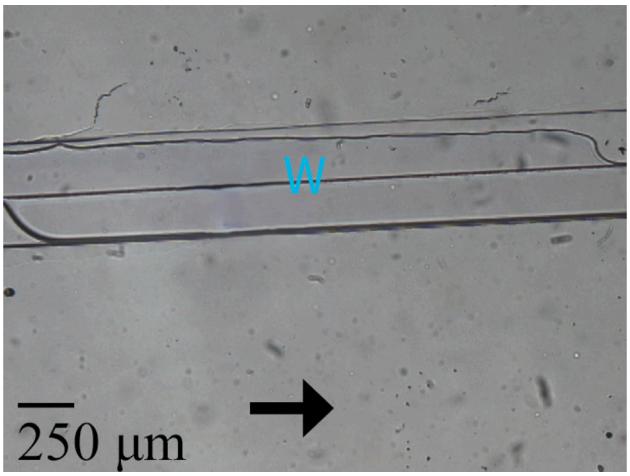

Fig. 4. A mixed regime is observed in a step channel when initialized at a high flow rate. The dyed fluid is water (the regions corresponding to the letter W) and the colourless fluid is Novec.

by adding a forcing term based on the Continuum Surface Force (CSF model) described by Brackbill et al. [38] to the Navier–Stokes equation. This is given by:

$$F = \frac{2\sigma\rho\kappa\nabla\alpha}{\rho_1 + \rho_2} \tag{3}$$

where σ is the interfacial tension coefficient and κ the curvature.

This term is known to induce spurious currents in VOF because the Young–Laplace relation involving the pressure difference and surface tension is not exactly satisfied [39,40]. While this is fine for higher Capillary numbers, simulations at low Capillary numbers are an issue as the interfacial forces are high, so the errors associated with the term are more pronounced. For this reason, the simulations will only be used to supplement the experiments and point towards the direction of future research rather than capture the entire range of flow phenomena.

3. Step vs standard channel

The experiments are performed on five different channels as discussed in Table 2. First, we focus on the differences between the step and standard channel for the same dimensions. The observed flow regimes are elucidated and compared for both channels, followed by the flow maps showing the differences in flow regimes. Then, we perform VOF simulations to visualize the differences between the two channels.

3.1. Flow regimes

In this section, we characterize the experimentally observed flow regimes in both the standard and step channels of width 500 μm. The regimes are classified based on their behaviour across the entire channel — inlet, main channel and outlet. This is slightly different from other papers which only consider the inlet and main channel [9,10,12]. Including the outlet provides a rounded description of all the flow phenomena occurring in the channel, and it is especially useful when we consider LLE applications where leakage plays a significant role. Based on the kind of regime, we show the flow phenomena near the inlet, main channel, or the outlet. For the standard channel, the following regimes are observed for various Capillary numbers and shown in Fig. 5:

1. *Slug Flow:* This flow regime generally occurs at low Capillary numbers ($Ca = 10^{-6} - 10^{-5}$), where interfacial forces are dominant [9,12]. In this regime, the dispersed phase occupies the entire channel and obstructs the flow of the continuous phase. Eventually, the pressure of the continuous phase builds up and leads to the shearing of the dispersed phase in the form of slugs as shown in Fig. 5(a) [41].
2. *Parallel Breakup Flow:* Here, the two fluids flow alongside each other in the main channel (Fig. 1(a)), but the inertial forces are not strong enough to maintain this configuration for the rest of the channel, so the parallel flow breaks up to form droplets in the main channel. [42] (Fig. 5(b)). This regime occurs at Ca number larger than those for slug flow (Ca of $O(10^{-5})$, where the flow rates of the two fluids are roughly comparable, although it is observed in some cases that the flow rate of the continuous phase is considerably larger than the dispersed phase. The inertial forces of the continuous phase seem to play a larger role in this regime, and this was also observed to be the case in the T-channel experiments of Zhao et al. [43].
3. *Parallel Flow with Leakage and Pinching:* This regime generally occurs at Ca number larger than that observed in Parallel Breakup Flow at comparable flow ($Ca = 10^{-5} - 8\times10^{-4}$). The exceptions to the rule are when the dispersed flow rates are much lesser than the continuous flow rates. The two phases flow alongside each other for the whole length of the channel, but the continuous phase “pinches" the dispersed phase at the entrance of the main channel as shown in Fig. 5(c), i.e, the dispersed phase is pushed slightly upwards by the continuous phase, after which the dispersed phase restores the original interface position. The interface position keeps varying near the inlet, which is why this phenomenon is classified separately from Parallel Flow with Leakage. At the end of the rectangular channel, either the continuous or dispersed phase leaks into the outlet of the other as in Fig. 5(e).
4. *Wavy Parallel Flow:* In this case, the two phases move alongside each other but the interface is not straight as in the previous two cases but wavy and unstable as the position of the interface changes with time (Fig. 5(d)). This regime occurs at Ca number larger than Parallel Flow with Pinching but smaller than Parallel Flow with Leakage (Ca of $O(10^{-3})$). It is only observed for a small range of Ca number, with the flow rates of the two phases being comparable.
5. *Parallel Flow with Leakage:* This is similar to the previous regime, except that it occurs at a higher Ca number ($Ca > 10^{-3}$) without any pinching (Fig. 5(e)). The position of the interface remains more or less the same throughout the channel barring the region near the outlet as the inertial forces are now large enough to sustain this regime [9,12,42,43]. The flow rates of the two phases are comparable here and leakage is observed here as well.

When it comes to the step channel, the flow regimes have not been previously classified in the literature to the author’s knowledge. Thus, the results presented in this research might be useful for further studies on step channels. The observed flow regimes in the step channel are shown in Fig. 6 and classified as follows:

1. *Stable Parallel Flow*: As shown in Fig. 6(a), the two fluids move alongside each other in parallel, but unlike the standard design, the interface is located exactly in the middle of the channel without any leakage, and this is the key reason why this kind of channel is employed in radioisotope extraction [28,44]. Surprisingly, this regime is observed at low Ca numbers in contrast to the standard channel ($Ca < 5 \times 10^{-5}$).
2. *Parallel Flow with Leakage and Pinching*: Similar phenomenon to that described for the standard channel, with leakage being observed at the outlet and pinching at the inlet. This phenomenon is observed for large Ca numbers at comparable flow rates. (Fig. 6(b), $Ca > 10^{-4}$)

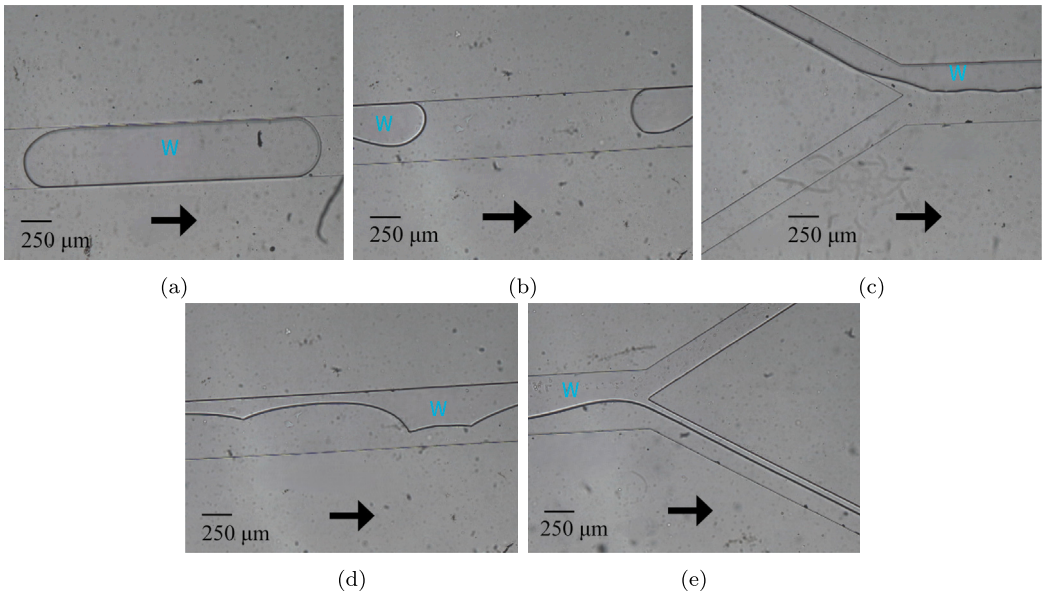

Fig. 5. Flow regimes observed in a standard channel for an HFE-Water mixture. The colourless fluid is HFE and the dyed fluid is water as indicated by the 'W'. (a) Slug Flow, (b) Parallel Breakup Flow, (c) Parallel Flow with Leakage and Pinching, (d) Wavy Parallel Flow, (e) Parallel Flow with Leakage.

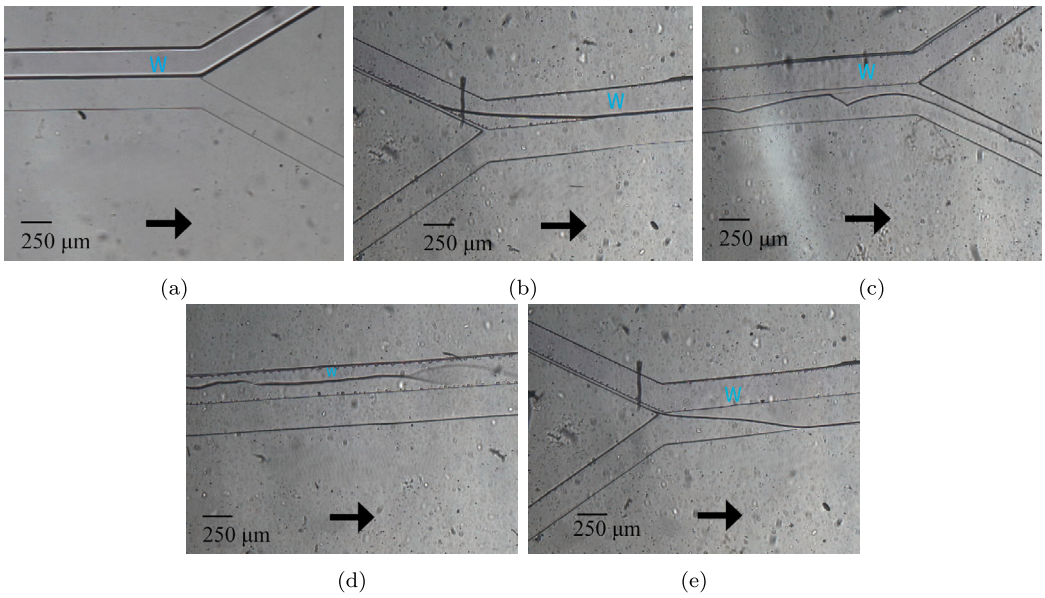

Fig. 6. Flow regimes observed in a step channel for an HFE-Water mixture. The colourless fluid is HFE and the dyed fluid is water as indicated by the 'W'. Water is located in the top and shallower section. (a) Parallel Flow, (b) Parallel Flow with Leakage and Pinching (c) Parallel Flow with Leakage (d) Parallel Breakup Flow (e) Complete Wetting.

3. *Parallel Flow with Leakage*: This regime is not observed frequently, and thus it is difficult to describe a trend for this regime (Fig. 6(c)), but it is similar to that observed for the standard channel in Fig. 5(e).
4. *Parallel Breakup Flow*: As with the standard channel, parallel flow breaks down to form droplets, but these droplets only occupy the shallow section and do not penetrate the deeper section (Fig. 6(d)). This regime generally occurs for larger continuous phase Ca numbers (Ca_n) and dispersed phase Ca numbers (Ca_w) as compared to stable parallel flow ($Ca_n/Ca_w \approx 10$).
5. *Complete Wetting*: When the flow rate of the continuous or dispersed phase is much larger compared to the other fluid (O(100) larger), one fluid completely wets the channel, and the other fluid only pinches the interface from time to time (Fig. 6(e)).

3.2. Flow maps

From the flow regimes discussed in the above section, we can clearly spot some differences between the regimes observed in the standard and step channels. To visualize these differences, we plot all the flow regimes on flow maps for the two channels based on the Capillary number in Fig. 7.

The clearest indication of the influence of geometry can be seen in the onset of parallel flow for either of the channels. At low Ca numbers where interfacial forces are dominant, stable parallel flow occurs in the step channel, whereas slug or parallel breakup flow is observed in the standard channel at the same Capillary number. Additionally, no leakage is also observed in the step channel, which points to the role of geometry and interfacial forces in stabilizing parallel flow. Slug flow is also never observed in the step channel for this width. At higher Ca numbers, the step channel gives similar results to the standard channel

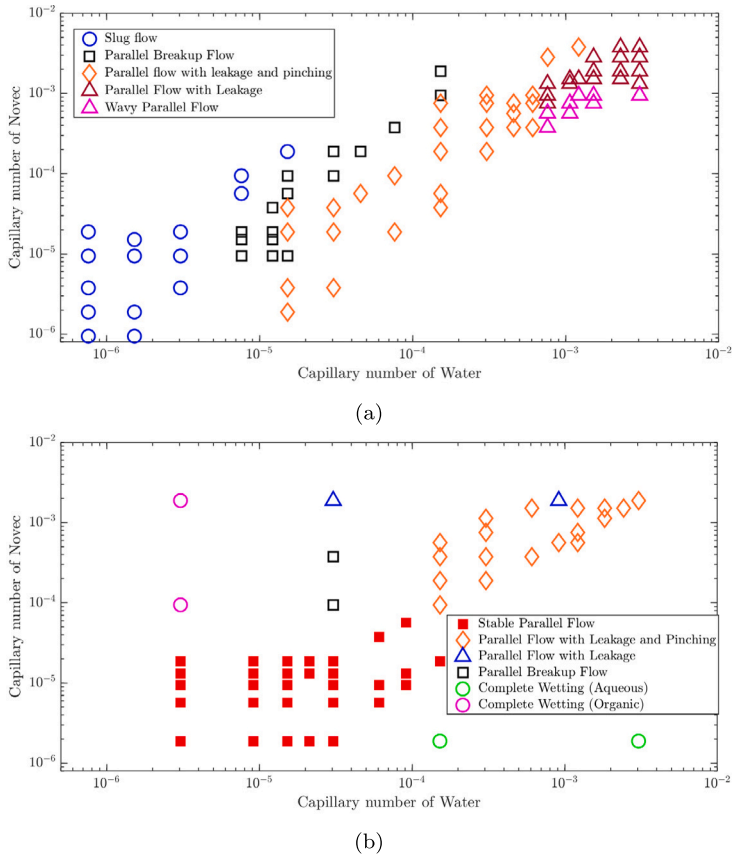

Fig. 7. Flow map for (a) Standard channel #1, (b) Step channel #2. Refer to Table 2 for channel details.

with parallel flow and leakage being the dominant regime, although pinching is more common in the step channel.

3.3. VOF simulations

To further understand how the channel design influences flow phenomena, we conduct VOF simulations to visualize fluid behaviour in such channels better. We compare slug flow in a standard channel with stable parallel flow in a step channel in order to shed some light on the role of interfacial tension in obtaining stable parallel flow in the step channel.

One problem associated with VOF is the presence of large spurious velocities that are generated at low Ca numbers ($Ca < 10^{-3}$) [39,45]. This was discussed in greater detail in a previous paper [45], where the velocities introduced by the CSF term mentioned in Eq. (3) were found to be much larger than the fluid velocities at low Ca numbers. These spurious velocities could influence the nature of the simulated flow regime. The flow maps in Figs. 7(a) and 7(b) clearly show many possible flow regimes at lower Capillary numbers. Therefore, we first check whether VOF is able to capture stable parallel flow in a step channel before we compare the regimes in a step and standard channel.

To validate the model, we run simulations for the Zinc Nitrate–chloroform mixture in a step channel as described by Trapp et al. [46]. Here chloroform, the wettable fluid, is located in the shallower section. In this setup, we obtain parallel flow as observed in the experiments at a flow rate of 1 μL/min (Fig. 8).

Next, we run simulations on Channel #2 at $(Ca_n, Ca_w) = (1.5 \times 10^{-5}, 3 \times 10^{-5})$, where stable parallel flow is expected (Fig. 7(b)). Novec is always located in the deeper section of the channel, similar to the experiments. The subscripts n and w correspond to Novec and water respectively. A reduced length of 2 mm is used in the simulations for the main channel to save computational time. A reduced length has been used in many simulations involving Y-Y and T-T channels as it was found to have little impact on the simulation results [15,47–49]. This was found to be true even in our simulations of the step channel, where the same flow regimes were obtained at lengths of 1.2 cm and 2 mm. Grid convergence was obtained at 5 μm so this was taken to be the grid length. Velocity boundary conditions were applied at the two inlets and pressure boundary conditions were applied at the two outlets. At the boundaries, the no-slip boundary condition and a wetting boundary condition corresponding to the contact angle are applied. The properties of the fluids are the same as that described in Table 1.

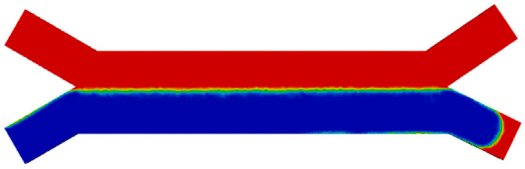

Fig. 8. Stable parallel flow for a Zinc Nitrate–chloroform mixture in channel #2 at a flow rate of 1 μL/min as observed in the experiments of Trapp et al. [46] The red fluid is Zinc Nitrate solution and the blue fluid is chloroform.

A hydrophilic channel is used in these simulations instead of the hydrophobic channels used in the experiments described in the previous sections. Parallel flow is observed for this setup as shown in Fig. 9(a). The reason for this is that parallel flow is not observed in the hydrophobic case (Fig. 9(b)). This implies that VOF is unable to capture certain phenomena in a step channel, but can simulate parallel flow in a step channel at low Capillary numbers. However, since we are mainly interested in the underlying phenomena of the flow regime, we therefore perform the simulations on a hydrophilic channel itself. The purpose of these simulations is not to capture the flow map observed in the experiments, but to understand why parallel flow is observed

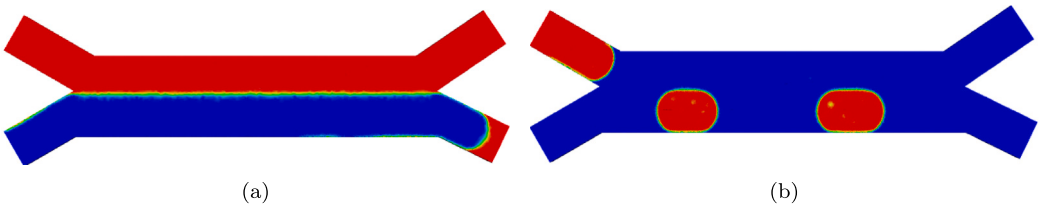

Fig. 9. VOF simulations for Water–Novec mixture in channel #2 at $(Ca_n, Ca_w) = (1.5 \times 10^{-5}, 3 \times 10^{-5})$, with a (a) Hydrophilic surface (b) Hydrophobic surface. The blue fluid is Novec and the red fluid is water, with Novec being located in the deeper section at the bottom half of the channel.

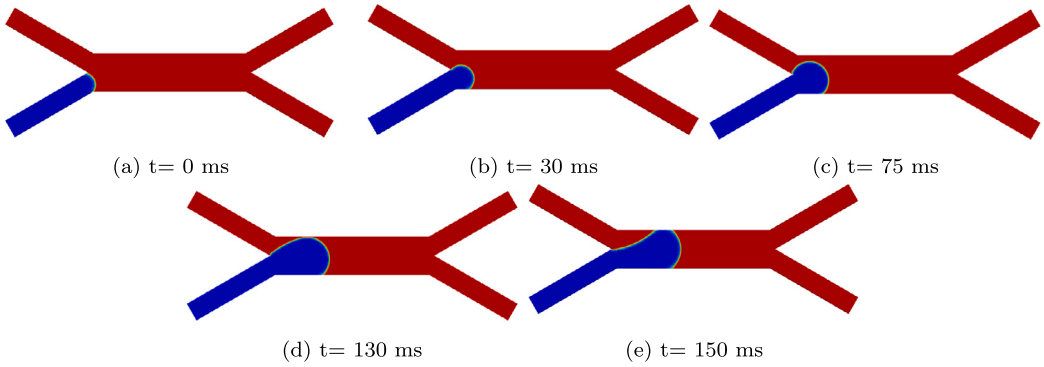

Fig. 10. Flow development in a standard channel at $Ca_w = 8 \times 10^{-5}$. The blue fluid is Novec and the red fluid is water.

Table 3
Channel Dimensions. The depth of the shallow channel is fixed at 20 μm and Novec is located in the deep channel. The walls are hydrophilic.

Type	Length (mm)	Width (μm)	Depth of deeper channel (μm/ l.u)	λ
Standard	1	200	20	1
Step	1	200	40	2

at such low Ca numbers, contrary to the results observed in a standard channel. Since stable parallel flow was also captured in the hydrophilic channel of Trapp et al. [46] at low flow rates, we can expect parallel flow to be the dominant regime at low Ca numbers regardless of the wettability. Obviously, if one aims to reproduce the flow maps shown in Fig. 7, a thorough benchmarking is necessary, and for this, the simulation models need to be studied in greater detail using techniques proposed by Ierardi et al. [50] to reduce the spurious velocities.

Since the purpose of the simulations is to qualitatively study the flow phenomena in the two different channels and not to reproduce the flow maps, we work with a channel of a similar geometry but with smaller dimensions for both the step and standard designs as described in Table 3 to reduce the computational time. In Section 2.4, we mentioned that the standard channel was initialized with the continuous phase occupying the entire domain and the dispersed phase introduced into one inlet. The simulations here are initialized similarly, with Novec being introduced from the deeper (bottom) inlet and water occupying the entire domain. Since we wish to compare the flow development in both the step and standard channels, the step channel is also initialized similarly. This initialization was found to have no impact on the simulated flow regime.

The regime observed in a standard channel is compared with stable parallel flow in a step channel at $(Ca_w,\ Ca_n) = (8 \times 10^{-5},\ 9.9 \times 10^{-5})$ by plotting the flow development in both channels along with the variations in pressure as the flow develops. The various stages of flow development for each channel are shown in Figs. 10 and 11. We measure the pressures of the aqueous and organic phases at two nodes located near the channel intersections (Fig. 1(a)) on either side of the interface respectively. The evolution of pressure across the time period is plotted for both channels in Fig. 12.

In the case of the standard channel, we can see that the aqueous (continuous) pressure keeps increasing over time, though the degree of increase varies. The aqueous pressure gradually increases as the organic (dispersed) phase enters and fills the main channel (Fig. 10(b)), after which a steep increase is observed as the organic phase blocks the flow of the aqueous phase (Figs. 10(c), 10(d)). A steep increase in the aqueous pressure was also observed in the blocking phase in the results of Lei et al. [41], after which the aqueous pressure drops due to the shearing of the organic phase by the aqueous phase to form a slug. Slug formation, however, is not observed in our case, so we still observe an increase in pressure, though the slope is less steep. The interface is deformed to form a more convex shape (Fig. 10(e)) as the aqueous phase pushes the organic phase towards the outlet.

The Novec pressure decreases until the period where the aqueous pressure sharply increases (Fig. 10(c)), after which it roughly remains constant, similar to the expected trend for the blocking stage [41]. If a slug was formed, a slight increase in the organic pressure would be observed.

In the case of the step channel, Novec enters the deeper section (Fig. 11(a)) and moves parallelly to water. Parallel flow is constantly maintained as Novec progresses through the channel without any changes in the position of the interface (Figs. 11(b), 11(c)). This is reflected in the pressure plot, with the aqueous and organic pressure remaining constant with time after the initial increase once Novec enters the main channel. The pressure is lower in magnitude than in the standard channel due to reasons related to the different flow regimes. In the case of parallel flow, both the aqueous and organic phases occupy half the channel area, whereas, for slug flow, both phases occupy the entire channel area. The larger pressure for slug flow is related to the increased area.

A constant pressure corresponds to a stable interface, as fluctuations in the fluid pressure result in the waviness of the interface. As discussed during the experimental results, the interfacial tension aids in stabilizing parallel flow at such low Capillary numbers. Since the inertial and viscous forces are very small, the interfacial tension guides the fluids into their respective channels. A strong interfacial force ensures that the fluid interface remains unperturbed for the entire duration of the flow in a step channel as the Laplace pressure balances the pressure drop due to viscous forces [21].

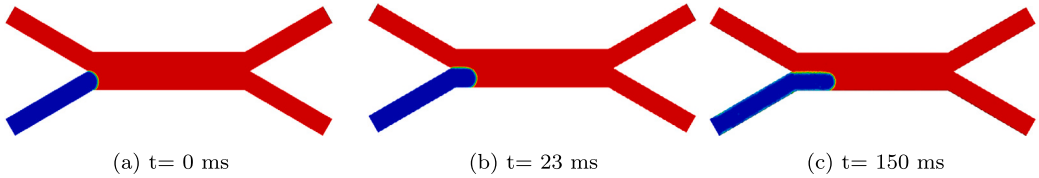

Fig. 11. Flow development in a step channel at $Ca_w = 8 \times 10^{-5}$. The blue fluid is Novec and the red fluid is water, with the deeper section located at the bottom half of the channel. The velocities of the two fluids are equal.

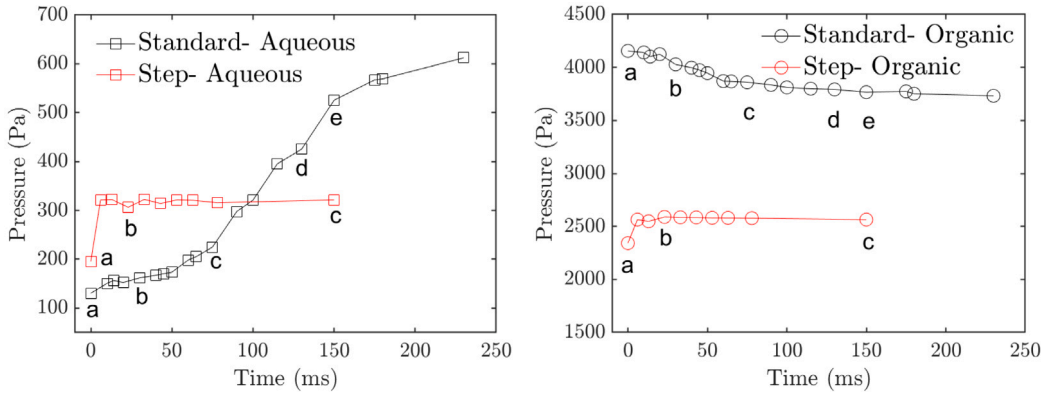

Fig. 12. Evolution of the pressure in the (a) Aqueous phase (b) Organic phase in both the channels. The letters in the plot correspond to the times shown in Figs. 10 and 11.

To summarize, the pressure development in a standard and step channel corresponds to the contrasting regimes observed at low Ca numbers. While the pressure keeps varying in a standard channel to correspond to slug formation, constant pressure in the step channel corresponds to stable parallel flow.

4. Influence of geometric dimensions in the step channel

To further understand the behaviour of fluids in a step design, we work with step channels with different dimensions. Many studies have been conducted on the effect of aspect ratio ($\Psi = W/H$) on the formation of droplets and the subsequent transition from droplet/slug flow to other regimes in standard channels [51–54]. The aspect ratio (Ψ) was found to affect the development of droplets, droplet frequency and onset of jetting or parallel flow. Some papers have also looked into the effect of the hydraulic diameter on the overall flow map [9,30]. All these studies have been conducted only on channels with symmetric cross-sections (λ=1).

A clearer comprehension of fluid behaviour in the step design is only possible when we look into the impact of Ψ and the degree of asymmetry (λ) on the flow patterns. $\lambda = 1$ corresponds to the standard channel, and we have already observed the differences in Fig. 7 when the channel is more asymmetric ($\lambda > 1$). Therefore, we study the effect of ψ on the flow map for the step channel by varying the width along with λ - a parameter unique to this step channel.

4.1. Flow regimes

In addition to the regimes that can be found in channels #1 and #2 (Table 2), the following regimes are observed in channels #3, #4 and #5 (Fig. 13):

1. *Unstable Parallel Flow*: This regime starts with fluids flowing alongside each other, but the interface position is never stable, and the dispersed phase even detaches sometimes, after which it forms a wavy parallel flow-like pattern as shown in Fig. 13(a). Wavy interfaces are observed near the inlet of the channel while parallel flow with leakage are observed near the outlet. Channel #4 shows this regime which normally occurs when the flow rate of the continuous phase is much larger than the dispersed phase ($Ca_n/Ca_w \approx 10$).
2. *Parallel Breakup Flow with Pinching*: The pinching phenomenon accompanies the parallel breakup flow regime described in Section 3.1. As described earlier, the continuous phase pinches the dispersed phase near the inlet of the channel, and parallel flow breaks up to form droplets or slugs inside the main channel. This occurs in Channel #3 at a high Ca number (O(10^{-3}))with the flow rates of the continuous and dispersed phases being similar.
3. *Slug/Droplet Flow*: Like the regime observed in the standard channel in Section 3.1, the dispersed phase detaches in the form of slugs/droplets. The key difference observed in a step channel is that the slug only occupies half the width of the entire channel and never penetrates the deep channel as shown in Fig. 13(b). This regime occurs in Channels #3 and #5 at lower Ca_w and much larger Ca_n ($Ca_n/Ca_w \approx 20$, $Ca = 10^{-6} - 10^{-5}$).
4. *Intermittently Stable Parallel Flow*: As the name suggests, the flow regime alternates between stable parallel flow with complete separation and pinching with leakage at the outlet as shown in Fig. 13(c). Stable parallel flow without leakage is observed for a few seconds, after which the continuous phase pinches the dispersed phase near the outlet, and then the cycle continues. This regime occurs only in channel #5 at low Ca numbers (O(10^{-5}))with similar flow rates.
5. *Wavy Parallel Flow*: Similar to the regime described for the standard channel in Section 3.1, the interface is wavy and its position keeps shifting (Fig. 13(d)). The regime is only observed in channel #5 for a few values of the Ca number ($Ca = 3\times10^{-4} - 10^{-3}$).

4.2. Flow maps

The flow regimes for channels #3, #4 and #5 are visualized using flow maps based on the Capillary number of both phases in Fig. 14. As

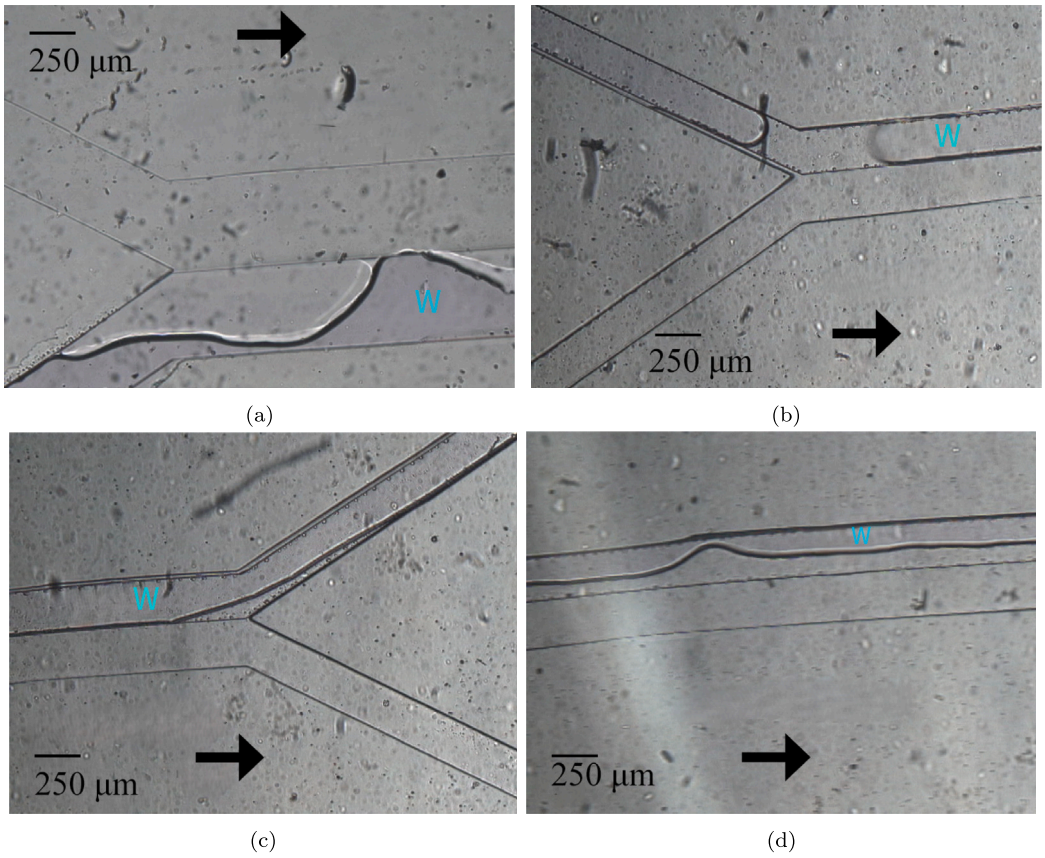

Fig. 13. Flow regimes observed in a step channel for an HFE-Water mixture. The colourless fluid is HFE and the dyed fluid is water, as indicated by the 'W'. (a) Unstable Parallel Flow, (b) Slug Flow (c) Intermittently Stable Parallel Flow (d) Wavy Parallel Flow.

hinted by the regimes discussed in the previous section, the width and λ clearly impact the nature of flow phenomena. In addition to the new regimes, the width also seems to have an influence on leakage, with the channel#4 flow map showing stable parallel flow for a broader range of Ca numbers as compared to channels #2 and #3 (Figs. 14(a), 14(b), 14(c)). Neither channels #2 nor #3 show any slug or droplet flow, but channel #4 does.

In the case of channel #5, the reduction in λ results in a flow map that is much more scattered than the other step channel flow maps. Channel #5 still favours parallel flow because of its asymmetric nature as can be seen in Fig. 14(c), but leakage and slug flow are also more commonly observed compared to other step channels. Thus, it is imperative to have a considerable height difference for stable parallel flow across a broad range of Ca numbers.

5. Generalized flow maps

In order to visualize the influence of the step channel dimensions more clearly, we plot the regions where stable parallel flow is observed for all the channels in Fig. 15. For the purposes of comparison, we also include the region where non-wavy parallel flow with leakage is observed in the standard channel just to visualize the stark contrast between the step and standard channel in terms of parallel flow. The figure shows a general pattern of stable parallel flow in step channels at low Ca numbers, which is in stark contrast to the results observed in standard channels. Aspect ratio and λ govern the range of Ca at which stable parallel flow is observed.

The channels which show the broadest range of stable parallel flow are channels #2 and #3. Stable parallel flow is observed even for higher Ca numbers in channel #3, whereas channel #2 shows stable parallel flow for lower Ca_n than that observed in channel #3. Decreasing the aspect ratio reduces leakage at higher Ca numbers, but the reduced width also results in more pinching at some lower Ca_n in channel #3.

A larger channel width in the case of channel #4 significantly reduces the region where stable parallel flow is observed. This might be related to the fact that the interfacial forces have to act over an increased surface area. Channel #5 shows the smallest region where stable parallel flow is observed, whereas the region for Channel #2 is much larger. This points to the role of λ on stable parallel flow, where the regimes were observed to be more scattered in Channel #5 as shown in Fig. 14(c)

To obtain an overall picture of the flow regimes and regions observed in the step channel, we plot a generalized flow map similar to the one described by Asadi-Sanghadi et al. [12] for all the step channels. Many papers have dedicated efforts to plotting such maps with numerous dimensionless number combinations [11,13,17], but Asadi-Sanghadi et al. found that their combination ($Ca^{0.31}We^{0.07}$) was applicable for a broader range of fluids when it comes to generalized flow maps. In the case of a step channel, however, we introduce a slight modification to the above relation. Figs. 7, 14 and 15 clearly point to the influence of λ and Ψ. To include this influence, we modify the combination slightly as follows:

$$Ca^{0.31}We^{0.07}\Delta^{0.07\mathrm{sgn}(\sin(\theta_f-\pi/2))} \tag{4}$$

where $\Delta = d_{h,n}/d_{h,w}$, with d_h being the hydraulic diameter and the subscripts n and w correspond to novec and water respectively. θ_f is the contact angle of the concerned fluid, which in this case is either water or novec. Δ is chosen both because it is dimensionless, so the dimensional analysis is unaffected, and because it encompasses the influences of both λ and Ψ. The power of 0.07 is chosen to correspond to that of the Weber number as the We·Δ is visualized as a modified Weber number for a step channel. We think such a modification is

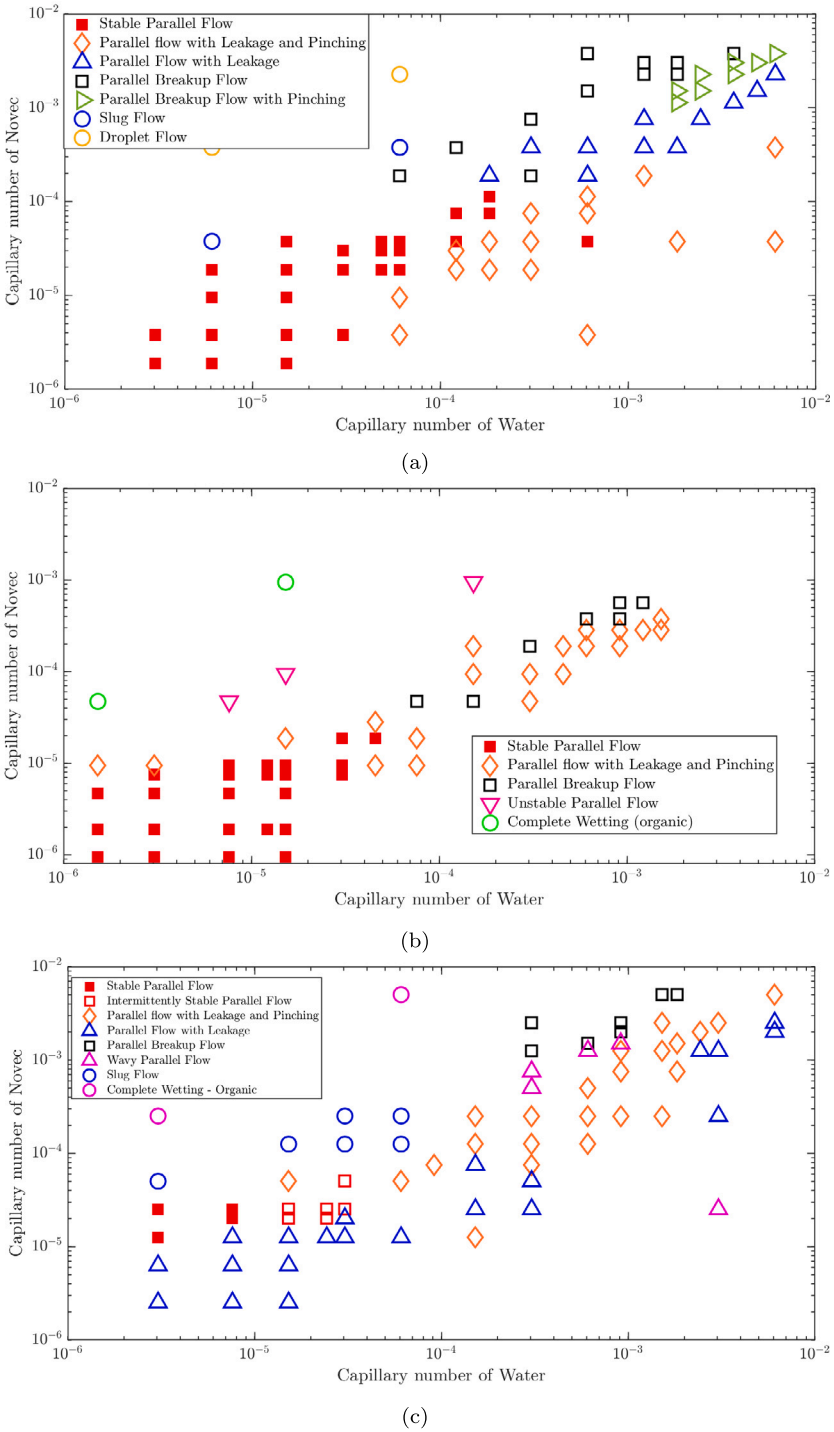

Fig. 14. Flow maps for step channels of different widths and λ.a) Channel #3, (b) Channel #4 (c) Channel #5. Refer to Table 2 for channel details.

necessary to include the effect of the step in pinning the interface. As Fig. 12 shows a strong influence of surface tension in the development of parallel flow in a step channel, we include the effect of contact angle in the form of a sgn function. From Figs. 7 and 14, we can see that the non-wetting fluid requires larger inertial forces for leakage or complete wetting to occur. Including the contact angle in the form of a sgn term is a way to account for this larger effort required by the non-wetting fluid. We plot the flow regimes of all the step channels using their combination in Fig. 16.

Based on the data, we propose to divide the generalized flow map into four regions: parallel, droplet/wetting, transition and mixed. The parallel region includes all possible configurations of parallel flow — leakage or no leakage. The droplet/wetting region includes both the complete wetting and slug/droplet regimes. Parallel breakup flow and wavy parallel flow – the intermediate regimes – form a part of the transition regimes. Finally, the mixed region, as the name indicates, contains a mixture of various regimes such as wetting, leakage and parallel. This region is located broadly in the right of Fig. 16. There are some outliers in the flow map which do not fall into their respective regions, but broadly, this is a useful division of the regions observed in the step channels.

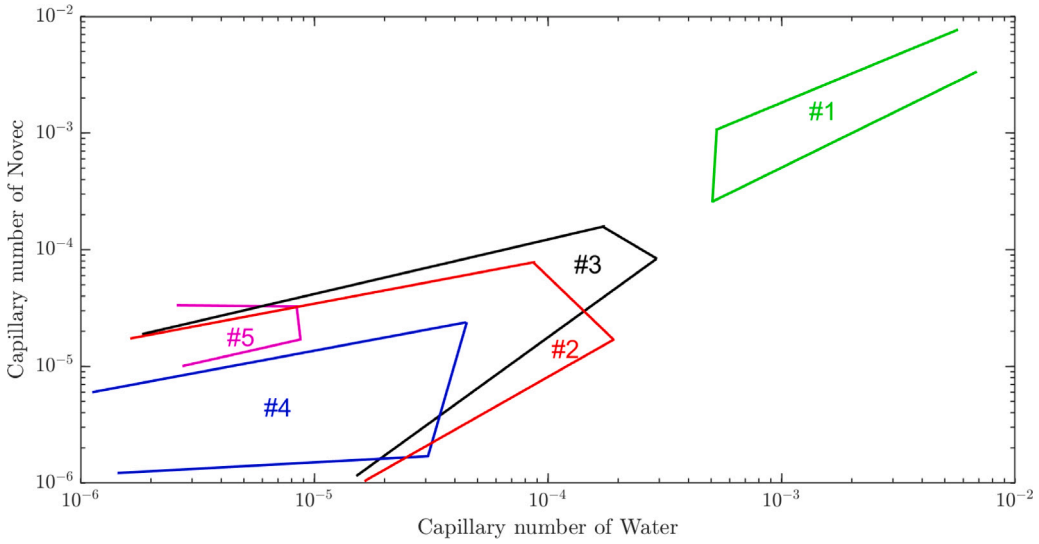

Fig. 15. Stable Parallel Flow regions for all step channels along with the region of 'Parallel Flow with Leakage' for the standard channel.

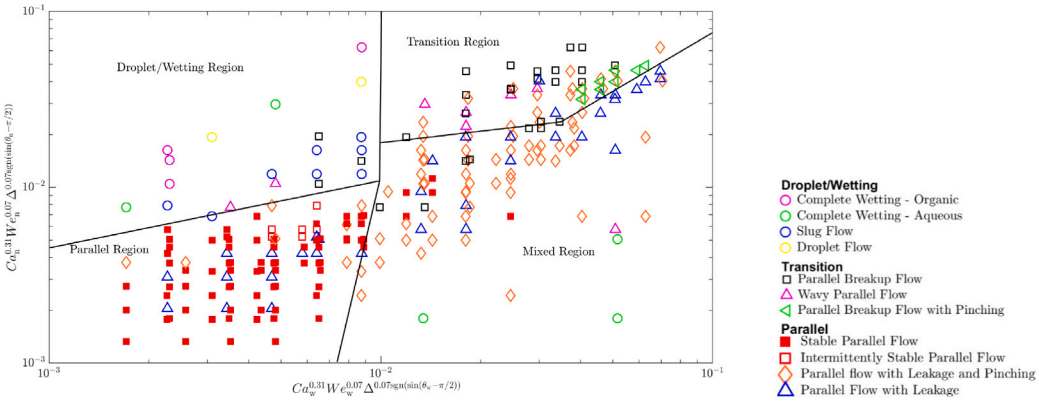

Fig. 16. Generalized flow map for the step channels using the dimensionless number combination from Asadi-Saghandi et al. and our modification (Eq. (4)) [12]. The map is divided into Parallel, Droplet/Wetting and Transition regions.

From Fig. 16, we can see that the dominant region corresponds to parallel flow. At lower $Ca^{0.31}We^{0.07}\Delta^{0.07sgn(sin(\theta_f-\pi/2))}$, stable parallel flow is observed and leakage is observed at higher $Ca^{0.31}We^{0.07}\Delta^{0.07sgn(sin(\theta_f-\pi/2))}$ with or without pinching. A lower Ca and We number correspond to a greater influence of interfacial tension, and the prominence of stable parallel flow at low $Ca^{0.31}We^{0.07}\Delta^{0.07sgn(sin(\theta_f-\pi/2))}$ reflects that.

When the $Ca^{0.31}We^{0.07}\Delta^{0.07sgn(sin(\theta_f-\pi/2))}$ of both fluids are high, we move towards the transition region in the flow map. Higher Ca numbers correspond to larger viscous forces and higher We numbers correspond to larger inertial forces. The boundary separating the parallel and transition regions might indicate the greater importance of inertial forces, especially at higher $Ca_n^{0.31}We_n^{0.07}$. Figs. 7(b), 14(a), 14(b) and 14(c) all show transition regimes at higher Ca_n, which is in contrast to a standard channel (Fig. 7), where transition regimes are observed intermediate to parallel and slug flow. More studies are needed on these transition regimes in step channels to see if the step induces more instabilities at higher $Ca^{0.31}We^{0.07}\Delta^{0.07sgn(sin(\theta_f-\pi/2))}$, leading to the breaking of the interface.

When the $Ca_n^{0.31}We_n^{0.07}\Delta^{0.07sgn(sin(\theta_n-\pi/2))}$ is at least 10 times larger than that of the dispersed phase and the $Ca_w^{0.31}We_w^{0.07}\Delta^{0.07sgn(sin(\theta_w-\pi/2))}$ smaller than 10^{-2}, droplets are observed, or one fluid completely wets the main channel. Droplets appear to be generated by a combination of interfacial forces (surface tension, wettability) and larger viscous forces of the continuous phase.

Finally, the mixed region corresponds to $Ca_w^{0.31}We_w^{0.07}\Delta^{0.07sgn(sin(\theta_w-\pi/2))}$ larger than 10^{-2}, and the $Ca_n^{0.31}We_n^{0.07}\Delta^{0.07sgn(sin(\theta_n-\pi/2))}$ is around 5–10 times smaller. Parallel flow with leakage and pinching appears to be the dominant regime in this region, where the viscous and inertial forces of the non-wetting fluid are larger than that of the wetting fluid. When the Ca and We numbers of the wetting fluid are small, complete wetting of the aqueous phase is observed in some cases, though more studies are needed in different channels to see if this is a common trend. Future studies in step channels should be geared towards transition and mixed regions as these are the areas that show the greatest variability.

To check the validity of our combination (Eq. (4)), we apply our combination to the results of Trapp et al. [46]. An important caveat is that the authors of that paper did not classify the flow regimes like ours, where the regimes are classified according to the flow phenomena observed across the entirety of the channel — inlet, main channel and outlet. They classified their regimes based only on the phenomena observed at the outlet, whether it is stable parallel flow, leakage or droplets. In this kind of classification, we can only check if the parallel region is accurately predicted. Therefore, we plot their results for our combination in Fig. 17.

Trapp et al. [46] used Zinc Nitrate and chloroform as their fluids in a channel of similar dimensions as Channel # 2 (Table 2). Here, Zinc Nitrate is the wetting fluid and occupies the channel of larger depth. As we can see from Fig. 17, the parallel region is accurately captured by

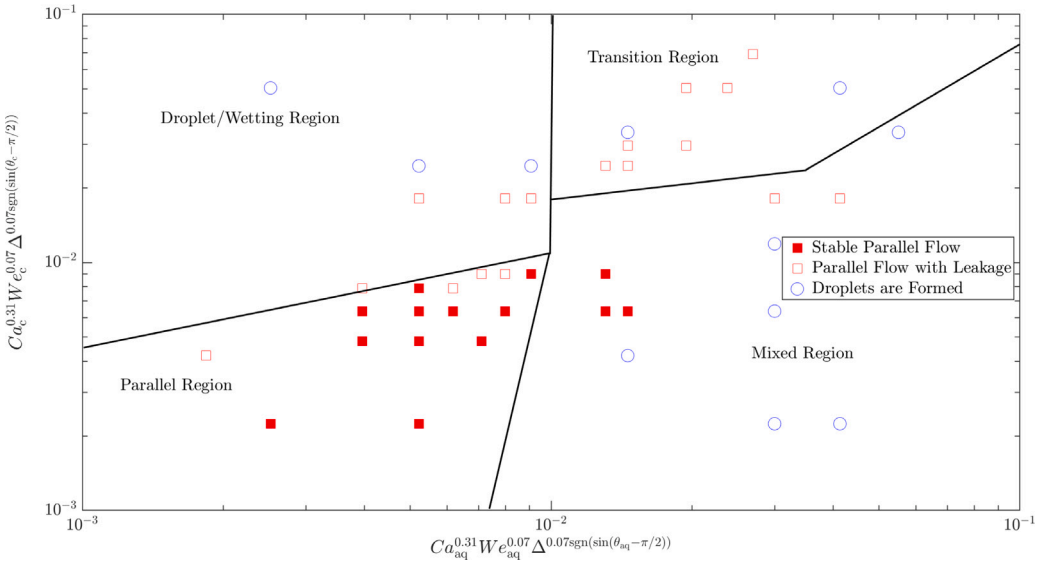

Fig. 17. Combination (4) is applied to the results of Trapp et al. [46] involving Zinc Nitrate (subscript 'aq') and Chloroform (subscript 'c') in a channel with dimensions similar to channel # 2 (Table 2). Zinc Nitrate is the wetting fluid and it occupies the channel of larger depth.

our combination. Whether other regions can be accurately described by this dimensionless number combination can only be confirmed by more experiments in step channels with different fluids.

6. Conclusion

In this paper, the step channel previously used in mass transfer applications has been studied in detail. This step channel is marked by a difference in depth across its two halves, i.e., one section is shallow and the other is deep. To understand the influence such a design might have on the flow phenomena, experiments were conducted on both the step channel and a standard channel – channel with uniform depth – and the various flow regimes were compared and plotted. It was found that the stable parallel flow was obtained at low Capillary numbers in the step channel, whereas slug and parallel breakup flow was obtained in the standard channel for the same set of Capillary numbers. Additionally, the interface was located exactly in the middle of the step channel with no leakage, and this could not be observed in the standard channel.

The flow phenomena observed in the step channel were compared and contrasted with those in the standard channel using VOF simulations. The pressure evolution at low Capillary numbers showed the variation of both aqueous and organic pressures in the standard channel as the organic phase enters into the filling and blocking stages. In contrast, the pressure of both the aqueous and organic phases was constant in the case of the step channel at the same Capillary number. The interfacial tension played a key role in maintaining the interface position and stable parallel flow along with the nature of the step design at such low Capillary numbers.

The step channel was further studied experimentally by varying the channel dimensions such as the width and step ratio, with flow maps being plotted for these channels as well. Reducing the step ratio resulted in a more scattered flow map, with stable parallel flow occurring less frequently and leakage being more common. A smaller width increased the range of Capillary numbers for which stable parallel flow was observed, while a larger width correspondingly reduced this range. Changing the dimensions also led to different regimes previously not observed in the first step channel such as slug flow or intermittently stable parallel flow. Plotting a generalized flow map for all these step channels revealed that the step design tends to favour parallel flow significantly more than other regimes, and this generalized flow map was found to be extensible for the results of Trapp et al. [46] in the case of the parallel region.

CRediT authorship contribution statement

Anand Sudha: Writing – review & editing, Writing – original draft, Visualization, Validation, Software, Methodology, Investigation, Formal analysis, Data curation, Conceptualization. **Albert Santoso:** Writing – original draft, Methodology. **Martin Rohde:** Writing – review & editing, Supervision, Resources, Project administration, Funding acquisition, Conceptualization.

Declaration of competing interest

The authors declare that they have no known competing financial interests or personal relationships that could have appeared to influence the work reported in this paper.

Acknowledgements

This publication is part of the Open Technology Programme (with project number 16913) financed by the Dutch Research Council (NWO). We thank Volkert van Steijn for the fruitful discussions.

Data availability

Data will be made available on request.

References

[1] K. Coats, R. Nielsen, M.H. Terhune, A. Weber, Simulation of three-dimensional, two-phase flow in oil and gas reservoirs, Soc. Pet. Eng. J. 7 (04) (1967) 377–388.
[2] A.A. Hyman, C.A. Weber, F. Jülicher, Liquid-liquid phase separation in biology, Annu. Rev. Cell. Dev. Biol. 30 (2014) 39–58.
[3] N. Assmann, A. Ładosz, P. Rudolf von Rohr, Continuous Micro Liquid-Liquid Extraction, Chem. Eng. Technol. 36 (6) (2013) 921–936, http://dx.doi.org/10.1002/ceat.201200557, URL https://onlinelibrary.wiley.com/doi/10.1002/ceat.201200557.
[4] A. Günther, K.F. Jensen, Multiphase microfluidics: from flow characteristics to chemical and materials synthesis, Lab Chip 6 (12) (2006) 1487–1503, http://dx.doi.org/10.1039/B609851G, URL http://xlink.rsc.org/?DOI=B609851G.
[5] J. Hanotu, H.H. Bandulasena, T.Y. Chiu, W.B. Zimmerman, Oil emulsion separation with fluidic oscillator generated microbubbles, Int. J. Multiph. Flow 56 (2013) 119–125.
[6] A. Ghaini, M. Kashid, D. Agar, Effective interfacial area for mass transfer in the liquid–liquid slug flow capillary microreactors, Chem. Eng. Process.: Process. Intensif. 49 (4) (2010) 358–366.

[7] A. Holbach, N. Kockmann, Counter-current arrangement of microfluidic liquid-liquid droplet flow contactors, Green Process. Synth. 2 (2) (2013) 157–167.

[8] A. Hibara, M. Tokeshi, K. Uchiyama, H. Hisamoto, T. Kitamori, Integrated multilayer flow system on a microchip, Anal. Sci. 17 (1) (2001) 89–93.

[9] M.N. Kashid, D.W. Agar, Hydrodynamics of liquid–liquid slug flow capillary microreactor: Flow regimes, slug size and pressure drop, Chem. Eng. J. 131 (1–3) (2007) 1–13, http://dx.doi.org/10.1016/j.cej.2006.11.020, URL https://linkinghub.elsevier.com/retrieve/pii/S1385894706005092.

[10] A.-L. Dessimoz, L. Cavin, A. Renken, L. Kiwi-Minsker, Liquid–liquid two-phase flow patterns and mass transfer characteristics in rectangular glass microreactors, Chem. Eng. Sci. 63 (16) (2008) 4035–4044, http://dx.doi.org/10.1016/j.ces.2008.05.005, URL https://linkinghub.elsevier.com/retrieve/pii/S000925090800256X.

[11] M. Kashid, L. Kiwi-Minsker, Quantitative prediction of flow patterns in liquid–liquid flow in micro-capillaries, Chem. Eng. Process.: Process. Intensif. 50 (10) (2011) 972–978, http://dx.doi.org/10.1016/j.cep.2011.07.003, URL https://linkinghub.elsevier.com/retrieve/pii/S0255270111001553.

[12] H. Asadi-Saghandi, J. Karimi-Sabet, S. Ghorbanian, S.M.A. Moosavian, Dimensionless analysis on liquid–liquid two-phase flow patterns in a numbered-up microfluidic device, Chem. Eng. J. 429 (2022) 132428, http://dx.doi.org/10.1016/j.cej.2021.132428, URL https://linkinghub.elsevier.com/retrieve/pii/S1385894721040067.

[13] Z. Cao, Z. Wu, B. Sundén, Dimensionless analysis on liquid-liquid flow patterns and scaling law on slug hydrodynamics in cross-junction microchannels, Chem. Eng. J. 344 (2018) 604–615, http://dx.doi.org/10.1016/j.cej.2018.03.119, URL https://linkinghub.elsevier.com/retrieve/pii/S1385894718304789.

[14] M. Kashid, A. Renken, L. Kiwi-Minsker, CFD modelling of liquid–liquid multiphase microstructured reactor: Slug flow generation, Chem. Eng. Res. Des. 88 (3) (2010) 362–368, http://dx.doi.org/10.1016/j.cherd.2009.11.017, URL https://linkinghub.elsevier.com/retrieve/pii/S0263876209003104.

[15] Z. Liu, Purifying radionuclides with microfluidic technology for medical purpose: Simulating multiphase flows inside a microfluidic channel with the phase field method, 2022.

[16] C.E. Brennen, Fundamentals of multiphase flow, Cambridge University Press, 2005.

[17] A.A. Yagodnitsyna, A.V. Kovalev, A.V. Bilsky, Flow patterns of immiscible liquid-liquid flow in a rectangular microchannel with T-junction, Chem. Eng. J. 303 (2016) 547–554, http://dx.doi.org/10.1016/j.cej.2016.06.023, URL https://linkinghub.elsevier.com/retrieve/pii/S1385894716308300.

[18] P. Martini, A. Adamo, N. Syna, A. Boschi, L. Uccelli, N. Weeranoppanant, J. Markham, G. Pascali, Perspectives on the Use of Liquid Extraction for Radioisotope Purification, Molecules 24 (2) (2019) 334, http://dx.doi.org/10.3390/molecules24020334, URL http://www.mdpi.com/1420-3049/24/2/334.

[19] A. Smirnova, K. Mawatari, A. Hibara, M.A. Proskurnin, T. Kitamori, Micro-multiphase laminar flows for the extraction and detection of carbaryl derivative, Anal. Chim. Acta 558 (1–2) (2006) 69–74, http://dx.doi.org/10.1016/j.aca.2005.10.073, URL https://linkinghub.elsevier.com/retrieve/pii/S0003267005018519.

[20] A. Hibara, M. Fukuyama, M. Chung, C. Priest, M.A. Proskurnin, Interfacial phenomena and fluid control in micro/nanofluidics, Anal. Sci. 32 (1) (2016) 11–21, http://dx.doi.org/10.2116/analsci.32.11, URL https://link.springer.com/10.2116/analsci.32.11.

[21] A. Aota, K. Mawatari, T. Kitamori, Parallel multiphase microflows: fundamental physics, stabilization methods and applications, Lab A Chip 9 (17) (2009) 2470, http://dx.doi.org/10.1039/b904430m, URL http://xlink.rsc.org/?DOI=b904430m.

[22] A. Pohar, M. Lakner, I. Plazl, Parallel flow of immiscible liquids in a microreactor: modeling and experimental study, Microfluid. Nanofluidics 12 (1–4) (2012) 307–316, http://dx.doi.org/10.1007/s10404-011-0873-7, URL http://link.springer.com/10.1007/s10404-011-0873-7.

[23] P. Vulto, S. Podszun, P. Meyer, C. Hermann, A. Manz, G.A. Urban, Phaseguides: a paradigm shift in microfluidic priming and emptying, Lab A Chip 11 (9) (2011) 1596, http://dx.doi.org/10.1039/c0lc00643b, URL http://xlink.rsc.org/?DOI=c0lc00643b.

[24] Y. Lu, Y. Xia, G. Luo, Phase separation of parallel laminar flow for aqueous two phase systems in branched microchannel, Microfluid. Nanofluidics 10 (5) (2011) 1079–1086, http://dx.doi.org/10.1007/s10404-010-0736-7, URL http://link.springer.com/10.1007/s10404-010-0736-7.

[25] S. Goyal, A.V. Desai, R.W. Lewis, D.R. Ranganathan, H. Li, D. Zeng, D.E. Reichert, P.J. Kenis, Thiolene and SIFEL-based microfluidic platforms for liquid–liquid extraction, Sensors Actuators B: Chem. 190 (2014) 634–644, http://dx.doi.org/10.1016/j.snb.2013.09.065, URL https://linkinghub.elsevier.com/retrieve/pii/S0925400513011064.

[26] F. Garbarino, K. Kistrup, G. Rizzi, M.F. Hansen, Burst pressure of phaseguide structures of different heights in all-polymer microfluidic channels, J. Micromech. Microeng. 27 (12) (2017) 125015, http://dx.doi.org/10.1088/1361-6439/aa97b7, URL https://iopscience.iop.org/article/10.1088/1361-6439/aa97b7.

[27] A. Hibara, S. Iwayama, S. Matsuoka, M. Ueno, Y. Kikutani, M. Tokeshi, T. Kitamori, Surface modification method of microchannels for gas-liquid two-phase flow in microchips, Anal. Chem. 77 (3) (2005) 943–947, http://dx.doi.org/10.1021/ac0490088, URL https://pubs.acs.org/doi/10.1021/ac0490088.

[28] G. Hellé, S. Roberston, S. Cavadias, C. Mariet, G. Cote, Toward numerical prototyping of labs-on-chip: modeling for liquid–liquid microfluidic devices for radionuclide extraction, Microfluid. Nanofluidics 19 (5) (2015) 1245–1257, http://dx.doi.org/10.1007/s10404-015-1643-8, URL http://link.springer.com/10.1007/s10404-015-1643-8.

[29] Y. Ban, Y. Kikutani, M. Tokeshi, Y. Morita, Extraction of Am(III) at the interface of organic-aqueous Two-layer flow in a microchannel, J. Nucl. Sci. Technol. 48 (10) (2011) 1313–1318, http://dx.doi.org/10.1080/18811248.2011.9711821, URL http://www.tandfonline.com/doi/abs/10.1080/18811248.2011.9711821.

[30] M. Darekar, K.K. Singh, S. Mukhopadhyay, K.T. Shenoy, Liquid–liquid two-phase flow patterns in Y-Junction microchannels, Ind. Eng. Chem. Res. 56 (42) (2017) 12215–12226, http://dx.doi.org/10.1021/acs.iecr.7b03164, URL https://pubs.acs.org/doi/10.1021/acs.iecr.7b03164.

[31] A. Farahani, A. Rahbar-Kelishami, H. Shayesteh, Microfluidic solvent extraction of Cd(II) in parallel flow pattern: Optimization, ion exchange, and mass transfer study, Sep. Purif. Technol. 258 (2021) 118031, http://dx.doi.org/10.1016/j.seppur.2020.118031, URL https://linkinghub.elsevier.com/retrieve/pii/S1383586620325041.

[32] Y. Yong, C. Yang, Y. Jiang, A. Joshi, Y. Shi, X. Yin, Numerical simulation of immiscible liquid-liquid flow in microchannels using lattice Boltzmann method, Sci. China Chem. 54 (1) (2011) 244–256, http://dx.doi.org/10.1007/s11426-010-4164-z, URL http://link.springer.com/10.1007/s11426-010-4164-z.

[33] A. Salim, M. Fourar, J. Pironon, J. Sausse, Oil–water two-phase flow in microchannels: Flow patterns and pressure drop measurements, Can. J. Chem. Eng. 86 (6) (2008) 978–988, http://dx.doi.org/10.1002/cjce.20108, URL https://onlinelibrary.wiley.com/doi/10.1002/cjce.20108.

[34] Z. Wu, Z. Cao, B. Sundén, Liquid-liquid flow patterns and slug hydrodynamics in square microchannels of cross-shaped junctions, Chem. Eng. Sci. 174 (2017) 56–66.

[35] I.-L. Ngo, S. Woo Joo, C. Byon, Effects of Junction Angle and Viscosity Ratio on Droplet Formation in Microfluidic Cross-Junction, J. Fluids Eng. 138 (5) (2016) 051202, http://dx.doi.org/10.1115/1.4031881, URL https://asmedigitalcollection.asme.org/fluidsengineering/article/doi/10.1115/1.4031881/372200/Effects-of-Junction-Angle-and-Viscosity-Ratio-on.

[36] C. Huang, J.A. Wippold, D. Stratis-Cullum, A. Han, Eliminating air bubble in microfluidic systems utilizing integrated in-line sloped microstructures, Biomed. Microdevices 22 (2020) 1–9.

[37] X.-B. Li, F.-C. Li, J.-C. Yang, H. Kinoshita, M. Oishi, M. Oshima, Study on the mechanism of droplet formation in T-junction microchannel, Chem. Eng. Sci. 69 (1) (2012) 340–351, http://dx.doi.org/10.1016/j.ces.2011.10.048, URL https://linkinghub.elsevier.com/retrieve/pii/S0009250911007627.

[38] J.U. Brackbill, D.B. Kothe, C. Zemach, A continuum method for modeling surface tension, J. Comput. Phys. 100 (2) (1992) 335–354.

[39] S. Popinet, Numerical Models of Surface Tension, Annu. Rev. Fluid Mech. 50 (1) (2018) 49–75, http://dx.doi.org/10.1146/annurev-fluid-122316-045034, URL https://www.annualreviews.org/doi/10.1146/annurev-fluid-122316-045034.

[40] A.Q. Raeini, M.J. Blunt, B. Bijeljic, Modelling two-phase flow in porous media at the pore scale using the volume-of-fluid method, J. Comput. Phys. 231 (17) (2012) 5653–5668, http://dx.doi.org/10.1016/j.jcp.2012.04.011, URL https://linkinghub.elsevier.com/retrieve/pii/S0021999112001830.

[41] L. Lei, Y. Zhao, X. Wang, G. Xin, J. Zhang, Experimental and numerical studies of liquid-liquid slug flows in micro channels with Y-junction inlets, Chem. Eng. Sci. 252 (2022) 117289, http://dx.doi.org/10.1016/j.ces.2021.117289, URL https://linkinghub.elsevier.com/retrieve/pii/S000925092100854X.

[42] Z. Liu, Purifying Radionuclides with Microfluidic Technology for Medical Purpose: Simulating multiphase flows inside a microfluidic channel with the phase field method (Ph.D. thesis), Delft University of Technology, 2022, http://dx.doi.org/10.4233/UUID:E1BEBCDD-185A-4515-B352-76D68F65ACE8, URL http://resolver.tudelft.nl/uuid:e1bebcdd-185a-4515-b352-76d68f65ace8.

[43] Y. Zhao, G. Chen, Q. Yuan, Liquid-liquid two-phase flow patterns in a rectangular microchannel, AIChE J. 52 (12) (2006) 4052–4060, http://dx.doi.org/10.1002/aic.11029, URL https://onlinelibrary.wiley.com/doi/10.1002/aic.11029.

[44] H. Karim, C. Castel, A. Lélias, A. Magnaldo, P. Sarrat, Kinetic study of uranium (VI) extraction with tributyl-phosphate in a stratified flow microchannel, Sep. Purif. Technol. 314 (2023) 123489, http://dx.doi.org/10.1016/j.seppur.2023.123489, URL https://linkinghub.elsevier.com/retrieve/pii/S1383586623003970.

[45] A. Sudha, M. Rohde, A modified forcing approach in the rothman–keller method for simulations of flow phenomena at low capillary numbers, Internat. J. Numer. Methods Fluids (2024).

[46] S. Trapp, A. Santoso, Y. Hounat, E. Paulssen, J.R. van Ommen, V. van Steijn, R.M. de Kruijff, Solvent extraction of ac-225 in nano-layer coated, solvent resistant pdms microfluidic chips, Scientific Reports 14 (1) (2024) 1–11.

[47] P. Kumar, M. Pathak, Dynamic wetting characteristics during droplet formation in a microfluidic T-junction, Int. J. Multiph. Flow 156 (2022) 104203, http://dx.doi.org/10.1016/j.ijmultiphaseflow.2022.104203, URL https://linkinghub.elsevier.com/retrieve/pii/S0301932222001823.

[48] P.F. Jahromi, J. Karimi-Sabet, Y. Amini, H. Fadaei, Pressure-driven liquid-liquid separation in Y-shaped microfluidic junctions, Chem. Eng. J. 328 (2017) 1075–1086.

[49] J. Jovanović, E.V. Rebrov, T.A.X. Nijhuis, M.T. Kreutzer, V. Hessel, J.C. Schouten, Liquid–liquid flow in a capillary microreactor: Hydrodynamic flow patterns and extraction performance, Ind. Eng. Chem. Res. 51 (2) (2012) 1015–1026, http://dx.doi.org/10.1021/ie200715m, URL https://pubs.acs.org/doi/10.1021/ie200715m.

[50] C. Ierardi, A.D. Torre, G. Montenegro, A. Onorati, F. Radaelli, L. Visconti, M. Miarelli, Modeling of two-phase flows at low capillary number with VoF method, Comput. & Fluids 252 (2023) 105772, http://dx.doi.org/10.1016/j.compfluid.2022.105772, URL https://linkinghub.elsevier.com/retrieve/pii/S0045793022003644.

[51] J.D. Wehking, M. Gabany, L. Chew, R. Kumar, Effects of viscosity, interfacial tension, and flow geometry on droplet formation in a microfluidic T-junction, Microfluid. Nanofluidics 16 (3) (2014) 441–453, http://dx.doi.org/10.1007/s10404-013-1239-0, URL http://link.springer.com/10.1007/s10404-013-1239-0.

[52] P. Garstecki, M.J. Fuerstman, H.A. Stone, G.M. Whitesides, Formation of droplets and bubbles in a microfluidic T-junction—scaling and mechanism of break-up, Lab A Chip 6 (3) (2006) 437, http://dx.doi.org/10.1039/b510841a, URL http://xlink.rsc.org/?DOI=b510841a.

[53] S.K. Jena, T. Srivastava, S.S. Bahga, S. Kondaraju, Effect of channel width on droplet generation inside T-junction microchannel, Phys. Fluids 35 (2) (2023).

[54] K. He, Z. Zhang, L. Zhang, W. Yuan, S.-M. Huang, Effects of geometrical confinement on the generation of droplets at microfluidics T-junctions with rectangle channels, Microfluid. Nanofluidics 27 (10) (2023) 67.